

Model-independent search for neutrino sources with the ANTARES neutrino telescope

A. Albert^b, M. André^c, M. Anghinolfi^d, G. Anton^e, M. Ardid^f,
 J.-J. Aubert^g, T. Avgitas^h, B. Baret^h, J. Barrios-Martíⁱ, S. Basa^j,
 V. Berting^g, S. Biagi^k, R. Bormuth^{l,m}, S. Bourret^h, M.C. Bouwhuis^l,
 R. Bruijn^{l,n}, J. Brunner^g, J. Bustog^g, A. Capone^{o,p}, L. Caramete^q,
 J. Carr^g, S. Celli^{o,p,r}, T. Chiarusi^s, M. Circella^t, J.A.B. Coelho^h,
 A. Coleiro^h, R. Coniglione^k, H. Costantini^g, P. Coyle^g, A. Creusot^h,
 A. Deschamps^u, G. De Bonis^{o,p}, C. Distefano^k, I. Di Palma^{o,p},
 C. Donzaud^{h,v}, D. Dornic^g, D. Drouhin^b, T. Eberl^{e,a}, I. El
 Bojadaini^w, D. Elsässer^x, A. Enzenhöfer^g, I. Felis^f, L.A. Fusco^{s,y},
 S. Galatà^h, P. Gay^{z,h}, S. Geiβelsöder^{e,a}, K. Geyer^e, V. Giordano^{aa},
 A. Gleixner^e, H. Glotin^{ab,ac}, T. Grégoire^h, R. Gracia Ruiz^h, K. Graf^e,
 S. Hallmann^e, H. van Haren^{ad}, A.J. Heijboer^l, Y. Hello^u, J.J.
 Hernández-Reyⁱ, J. Hößl^e, J. Hofestädt^e, C. Hugon^{d,ae},
 G. Illuminati^{o,p,i}, C.W James^e, M. de Jong^{l,m}, M. Jongen^l,
 M. Kadler^x, O. Kalekin^e, U. Katz^e, D. Kießling^e, A. Kouchner^{h,ac},
 M. Kreter^x, I. Kreykenbohm^{af}, V. Kulikovskiy^{k,ag}, C. Lachaud^h,
 R. Lahmann^e, D. Lefèvre^{ah}, E. Leonora^{aa,ai}, M. Lotzeⁱ,
 S. Loucatis^{aj,h}, M. Marcelin^j, A. Margiotta^{s,y}, A. Marinelli^{ak,al},
 J.A. Martínez-Mora^f, A. Mathieu^g, R. Mele^{am,ap}, K. Melis^{l,n},
 T. Michael^l, P. Migliozi^{am}, A. Moussa^w, C. Mueller^x, E. Nezri^j,
 G.E. Păvălaş^q, C. Pellegrino^{s,y}, C. Perrina^{o,p}, P. Piattelli^k, V. Popa^q,
 T. Pradier^{an}, L. Quinn^g, C. Racca^b, G. Riccobene^k, K. Roensch^e,
 A. Sánchez-Losa^t, M. Saldaña^f, I. Salvador^g, D. F. E. Samtleben^{l,m},
 M. Sanguineti^{d,ae}, P. Sapienza^k, J. Schnabel^e, F. Schüssler^{aj}, T. Seitz^e,
 C. Sieger^e, M. Spurio^{s,y}, Th. Stolarczyk^{aj}, M. Taiuti^{d,ae}, Y. Tayalati^{ao},
 A. Trovato^k, M. Tselengidou^e, D. Turpin^g, C. Tönnisⁱ, B. Vallage^{aj,h},
 C. Vallée^g, V. Van Elewyck^{h,ac}, D. Vivolo^{am,ap}, A. Vizzoca^{o,p},
 S. Wagner^e, J. Wilms^{af}, J.D. Zornozaⁱ, and J. Zúñigaⁱ

^aCorresponding author

^bGRPHE - Université de Haute Alsace - Institut universitaire de technologie de Colmar, 34 rue du Grillenbreit BP 50568 - 68008 Colmar, France

^cTechnical University of Catalonia, Laboratory of Applied Bioacoustics, Rambla Exposició, 08800 Vilanova i la Geltrú, Barcelona, Spain

^dINFN - Sezione di Genova, Via Dodecaneso 33, 16146 Genova, Italy

^eFriedrich-Alexander-Universität Erlangen-Nürnberg, Erlangen Centre for Astroparticle Physics, Erwin-Rommel-Str. 1, 91058 Erlangen, Germany

^fInstitut d'Investigació per a la Gestió Integrada de les Zones Costaneres (IGIC) - Universitat

- ^aPolitecnica de València. C/ Paranimf 1 , 46730 Gandia, Spain.
- ^bAix-Marseille Université, CNRS/IN2P3, CPPM UMR 7346, 13288 Marseille, France
- ^cAPC, Université Paris Diderot, CNRS/IN2P3, CEA/IRFU, Observatoire de Paris, Sorbonne
Paris Cité, 75205 Paris, France
- ^dIFIC - Instituto de Física Corpuscular (CSIC - Universitat de València) c/ Catedrático José
Beltrán, 2 E-46980 Paterna, Valencia, Spain
- ^eLAM - Laboratoire d'Astrophysique de Marseille, Pôle de l'Etoile Site de Château-Gombert,
rue Frédéric Joliot-Curie 38, 13388 Marseille Cedex 13, France
- ^fINFN - Laboratori Nazionali del Sud (LNS), Via S. Sofia 62, 95123 Catania, Italy
- ^gNikhef, Science Park, Amsterdam, The Netherlands
- ^hHuygens-Kamerlingh Onnes Laboratorium, Universiteit Leiden, The Netherlands
- ⁱUniversiteit van Amsterdam, Instituut voor Hoge-Energie Fysica, Science Park 105, 1098 XG
Amsterdam, The Netherlands
- ^jINFN -Sezione di Roma, P.le Aldo Moro 2, 00185 Roma, Italy
- ^kDipartimento di Fisica dell'Università La Sapienza, P.le Aldo Moro 2, 00185 Roma, Italy
- ^lInstitute for Space Science, RO-077125 Bucharest, Măgurele, Romania
- ^mGran Sasso Science Institute, Viale Francesco Crispi 7, 00167 L'Aquila, Italy
- ⁿINFN - Sezione di Bologna, Viale Berti-Pichat 6/2, 40127 Bologna, Italy
- ^oINFN - Sezione di Bari, Via E. Orabona 4, 70126 Bari, Italy
- ^pGéoazur, UCA, CNRS, IRD, Observatoire de la Côte d'Azur, Sophia Antipolis, France
- ^qUniv. Paris-Sud , 91405 Orsay Cedex, France
- ^rUniversity Mohammed I, Laboratory of Physics of Matter and Radiations, B.P.717, Oujda
6000, Morocco
- ^sInstitut für Theoretische Physik und Astrophysik, Universität Würzburg, Emil-Fischer Str. 31,
97074 Würzburg, Germany
- ^tDipartimento di Fisica e Astronomia dell'Università, Viale Berti Pichat 6/2, 40127 Bologna,
Italy
- ^uLaboratoire de Physique Corpusculaire, Clermont Univertsité, Université Blaise Pascal,
CNRS/IN2P3, BP 10448, F-63000 Clermont-Ferrand, France
- ^vINFN - Sezione di Catania, Viale Andrea Doria 6, 95125 Catania, Italy
- ^wLSIS, Aix Marseille Université CNRS ENSAM LSIS UMR 7296 13397 Marseille, France ;
Université de Toulon CNRS LSIS UMR 7296 83957 La Garde, France
- ^xInstitut Universitaire de France, 75005 Paris, France
- ^yRoyal Netherlands Institute for Sea Research (NIOZ), Landsdiep 4,1797 SZ 't Horntje (Texel),
The Netherlands
- ^zDipartimento di Fisica dell'Università, Via Dodecaneso 33, 16146 Genova, Italy
- ^{aa}Dr. Remeis-Sternwarte and ECAP, Universität Erlangen-Nürnberg, Sternwartstr. 7, 96049
Bamberg, Germany
- ^{ab}Moscow State University,Skobeltsyn Institute of Nuclear Physics,Leninskie gory, 119991
Moscow, Russia
- ^{ac}Mediterranean Institute of Oceanography (MIO), Aix-Marseille University, 13288, Marseille,
Cedex 9, France; Université du Sud Toulon-Var, 83957, La Garde Cedex, France
CNRS-INSU/IRD UM 110
- ^{ad}Dipartimento di Fisica ed Astronomia dell'Università, Viale Andrea Doria 6, 95125 Catania,
Italy
- ^{ae}Direction des Sciences de la Matière - Institut de recherche sur les lois fondamentales de
l'Univers - Service de Physique des Particules, CEA Saclay, 91191 Gif-sur-Yvette Cedex, France
- ^{af}INFN - Sezione di Pisa, Largo B. Pontecorvo 3, 56127 Pisa, Italy
- ^{ag}Dipartimento di Fisica dell'Università, Largo B. Pontecorvo 3, 56127 Pisa, Italy
- ^{ah}INFN -Sezione di Napoli, Via Cintia 80126 Napoli, Italy
- ^{ai}Université de Strasbourg, IPHC, 23 rue du Loess 67037 Strasbourg, France - CNRS,
UMR7178, 67037 Strasbourg, France
- ^{aj}University Mohammed V in Rabat, Faculty of Sciences, 4 av. Ibn Battouta, B.P. 1014, R.P.
10000 Rabat, Morocco
- ^{ak}Dipartimento di Fisica dell'Università Federico II di Napoli, Via Cintia 80126, Napoli, Italy

March 14, 2017

Abstract

A novel method to analyse the spatial distribution of neutrino candidates recorded with the ANTARES neutrino telescope is introduced, searching for an excess of neutrinos in a region of arbitrary size and shape from any direction in the sky. Techniques originating from the domains of machine learning, pattern recognition and image processing are used to purify the sample of neutrino candidates and for the analysis of the obtained skymap. In contrast to a dedicated search for a specific neutrino emission model, this approach is sensitive to a wide range of possible morphologies of potential sources of high-energy neutrino emission. The application of these methods to ANTARES data yields a large-scale excess with a post-trial significance of 2.5σ . Applied to public data from IceCube in its IC40 configuration, an excess consistent with the results from ANTARES is observed with a post-trial significance of 2.1σ .

1 Introduction

Since the recent discovery of a diffuse high-energy astrophysical neutrino flux by the IceCube Collaboration [1, 2, 3], neutrino astronomy has established itself as a new discipline. Due to the statistical limitations implied by a new observational tool that has just overcome its initial detection threshold, the spectral and spatial properties of the discovered flux are still not well constrained.

The high-energy starting event (HESE) analysis [2], which is most sensitive to the Southern sky but has a poor spatial resolution, measures a best-fit diffuse signal of $dN_\nu/dE \propto E^\Gamma$ with $\Gamma = -2.5$ [4]. The flux observed from the Northern Sky with a higher energy threshold of about 200 TeV in the muon channel exhibits a harder spectral index of about $\Gamma = -2.0$ [5].

A first analysis has shown that the spatial distribution of HESE events is consistent with an isotropic distribution [6]. However, there is some evidence for an excess at low galactic latitudes [7]. This finding is supported by the consistency of gamma-ray and neutrino spectra in the HESE sky region [8, 9], although ANTARES is already constraining this scenario [10]. The origin of the various contributions remains open, but a galactic contribution with a softer spectrum and an extragalactic contribution with a harder spectrum seem to be favoured [11].

Several analyses with the goal to reveal the origin of the astrophysical neutrinos have been performed. Time-integrated searches for point-like and extended bright sources by ANTARES [12], IceCube [13] and a joint search [14] exclude the possibility that the flux can be generated by a small number of bright sources. A first search employing a two-point correlation function with data from the ANTARES neutrino telescope [15] has neither found significant deviations from isotropy in the full-sky neutrino distribution nor

shown evidence for correlations with catalogues of various astrophysical objects. Likewise a two-point correlation and multipole analysis of IceCube skymaps confirmed that the assumption of a small number of bright sources is excluded [16]. Therefore, a distribution of many faint point-like or unexpected extended sources constitutes a promising hypothesis at this stage.

ANTARES [17] is the largest operational neutrino telescope in the Northern Hemisphere, located in the Mediterranean Sea ($42^{\circ}48'N$, $6^{\circ}10'E$) at a depth of 2475 m. Due to its location, it mainly observes the Southern sky in the upgoing muon channel and provides an excellent view on the Galactic Centre. Despite its much smaller instrumented volume compared to IceCube, it has an effective area for muon neutrinos which is comparable to that of the IceCube HESE analysis for energies around 100 TeV and even surpasses it for energies below about 60 TeV [18].

This paper introduces three independent new methods and the results obtained with them. The first two algorithms enhance the data selection and reconstruction process, while the third is a novel analysis method that uses the arrival directions of upgoing muon neutrinos recorded with the ANTARES neutrino telescope in 6 years of data taking. The goal of this analysis is to identify the most significant, spatially confined excess over the background of atmospheric neutrinos without relying on assumptions of any emission model of potential neutrino sources.

2 Signal identification

In order to distinguish events resulting from genuine neutrinos from the background of atmospheric muons that reach the telescope from above and generate about 10^6 times more events, cuts are placed on the direction reconstruction to select those that are consistent with an “upgoing” particle entering the telescope from below.

In this analysis a multivariate classification technique called “Random Decision Forest” (RDF)¹ [20] is used in addition to allow less strict cuts on the reconstruction quality, increasing the available statistics. The RDF operates on variables describing the topology and timing pattern of the light observed within ANTARES [21]. The output of this algorithm for a recorded event is an assignment to a predefined class. In this application the classes are “upgoing” and “downgoing”. The algorithm is trained on Monte Carlo simulations that incorporate the observed time-dependent data-taking conditions [22]. To improve the accuracy of the results, a two-step classification is used, where the first classification rejects only clearly downgoing signatures, while the second step is trained specifically to filter out those atmospheric muon events that generate patterns similar to the desired upgoing muon neutrinos. This technique reaches a rejection

¹The used implementation is forked from an open source version of alglib [19].

rate of $99.85\% \pm 0.12\%$ for downgoing atmospheric muons while preserving $81.7\% \pm 1.3\%$ of all charged current muon neutrino events (calculated for a spectrum following $E^{-2.0}$). Compared to a single stage RDF classification with a similar efficiency for upgoing neutrino events it reduces atmospheric muons by a factor of 20. Figure 1 shows the efficiency for upgoing muon neutrinos as a function of the neutrino energy.

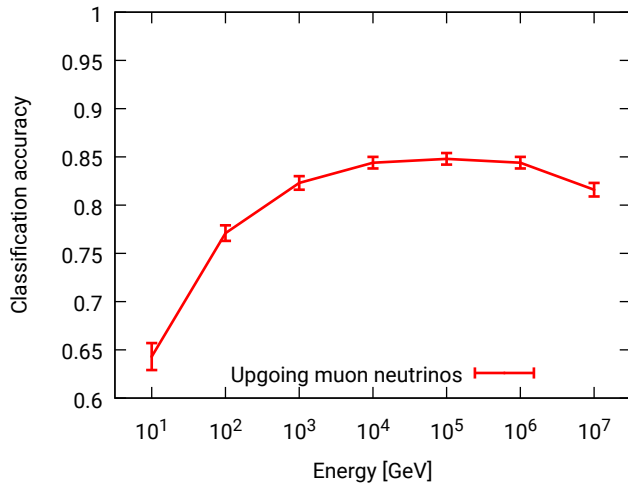


Figure 1: The classification accuracy (which also is the efficiency in this application) of the two step RDF classification for upgoing muon neutrinos versus energy for Monte Carlo simulations. The error bars indicate one standard deviation of statistical errors plus an estimate of the systematic error resulting from fluctuations in the training sample.

3 Direction reconstruction

A novel method called “Selectfit” is used to reconstruct the direction of neutrino candidates. Instead of applying one reconstruction algorithm for all neutrino candidates, Selectfit combines the results of multiple direction reconstruction algorithms, aiming to select the most precise result for each event. It combines four reconstruction algorithms previously used by ANTARES [23, 24, 25]. The selection is again performed by a Random Decision Forest using the reconstruction results (zenith and azimuth angle) as well as all available quality-related output parameters of the considered reconstruction algorithms as input variables.

In order to estimate the accuracy of the reconstruction for each event in a comparable way, Selectfit cannot just rely on the quality variable of the chosen algorithm. Instead it combines the results and quality parameters

of all considered algorithms using a RDF. The output of this second RDF are classes corresponding to bins of angular error ($< 0.1^\circ$, $< 0.2^\circ$, $< 0.4^\circ$, $< 0.8^\circ$, ...).

As illustrated in Figure 2, Selectfit either allows the angular error for a sample of neutrinos to be reduced or it can be used to increase the sample size for a given angular error. It increases the available statistics by at least 11% for any given accuracy. The benefit for small angular errors is

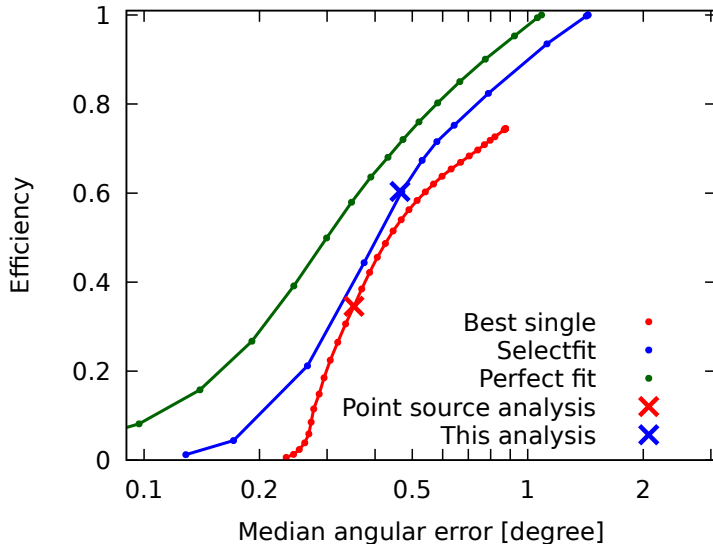


Figure 2: Comparison of the efficiency versus the median angular error of direction reconstruction algorithms. Every point of these curves is obtained for a different cut on the quality variables. Shown are the performance of the on average most accurate individual direction reconstruction algorithm [23] in red for cuts on its standard quality parameter and the novel method “Selectfit” with cuts on the estimated error class in blue. The green line shows the unreachable, hypothetical limit for the concept of Selectfit in this application. It is the performance if for every event the best available single reconstruction was chosen and the true angular uncertainty was used for the selection. All performances have been evaluated for a neutrino flux following an E^{-2} energy spectrum. The crosses indicate the cuts used for the single algorithm in [26] and for Selectfit in this analysis.

mainly due to the improved estimation of the angular error, whereas for less accurate reconstructions, the main benefit results from the eventwise selection from the four reconstruction methods [21].

Since a search for extended sources does not necessarily require the same angular precision as a point source search, a looser cut on the uncertainty of

the reconstruction is applied. For a flux with an energy spectrum of E^{-2} this results in a median angular uncertainty of 0.46° for the remaining sample. The cut for this analysis was chosen to yield a high statistics sample of muon neutrino candidates while reconstructing them accurately enough to match the 0.5° grid spacing used in the multiscale method, see Section 4.

4 Model-independent multiscale source search

The model-independent multiscale source search aims to identify the region of arbitrary position, size, shape and internal distribution with the most significant excess of neutrino events in the sky with respect to the background expectation.

Compared to a dedicated analysis searching for a specific hypothesis for the source of neutrino production, this method has a higher trial factor. On the other hand, being model-independent means it is insensitive to systematic uncertainties in source hypotheses and it can even detect unexpected sources or distributions of sources. More details on all steps of the computation can be found in [21].

4.1 The search grid

A discrete spherical grid² with a spacing of $\approx 0.5^\circ$ is used to evaluate the directions of the measured events. Figure 3 shows such a spherical grid with gridpoints in blue and 12000 randomly generated neutrino events in white. This number of neutrinos is close to the expectation for the data analysis and they are distributed according to the visibility of ANTARES. In order to better illustrate the steps of the analysis method, two artificial point sources with 12 and 18 events respectively have been added at a declination of -70° .

4.2 Counting

The search begins by counting the number of neutrinos located in a ring around each gridpoint. The inner radius of the ring is set according to the current search scale, with the outer radius of the ring always being 0.5° larger. The search evaluates 180 different scales from 0.0° up to 90.0° in steps of 0.5° . This evaluation is performed individually for each scale on a full spherical grid. A visualisation of the counting scheme is depicted in Figure 4. Counting the number of neutrinos located within these rings results in one value N per gridpoint and per scale. For three of the scales the results of this counting on the example from Figure 3 can be seen in Figure 5. Note that, unless stated otherwise, in Figure 5 and all following

²The grid consists out of 165016 gridpoints

similar Figures, the colour code is readjusted between the different scales to match the range of values on each sphere.

4.3 Poisson probabilities

The next step is to calculate the Poisson probability $P(N, \lambda)$ for each of the observed values N . The expected mean number λ for each gridpoint is estimated by pseudo experiments using scrambled events. The scrambling is achieved by using the time of another randomly selected neutrino event when computing equatorial from local coordinates. This results in randomised distributions that preserve the characteristics of the actual data taking, for instance the distribution of the declinations or the efficiency of the data taking versus time. The computed Poisson probabilities are then modified according to Equation 1, where $P(x \geq N, \lambda)$ is the probability for a value equal or greater than the observed one.

$$R' = \log_{10}\left(\frac{1}{P(x \geq N, \lambda)}\right) \quad (1)$$

A lowpass filter³ is applied to the spheres after that to reduce the influence of statistical fluctuations. These smoothed R' values are called R . The search spheres after these computations are shown in Figure 6.

4.4 Segmentation I

The next step aims to focus on potentially relevant information and to remove background fluctuations. In general, this task, well known in the field of computer vision, is called segmentation. Here it is performed using a simple threshold θ . Values below the threshold, e.g. less pronounced fluctuations, are removed. The threshold θ is derived and applied to each scale independently, based on the histogram of the R values of this scale. Figure 7 illustrates the details how the threshold is obtained from the histogram. The outcome of this step at a gridpoint p is given by:

$$E_p = \begin{cases} R_p, & R_p \geq \theta \\ 0, & R_p < \theta \end{cases} \quad (2)$$

The result after the segmentation is shown in Figure 8.

³Implemented as normalised box filter (averaging of nine neighbouring gridpoints)

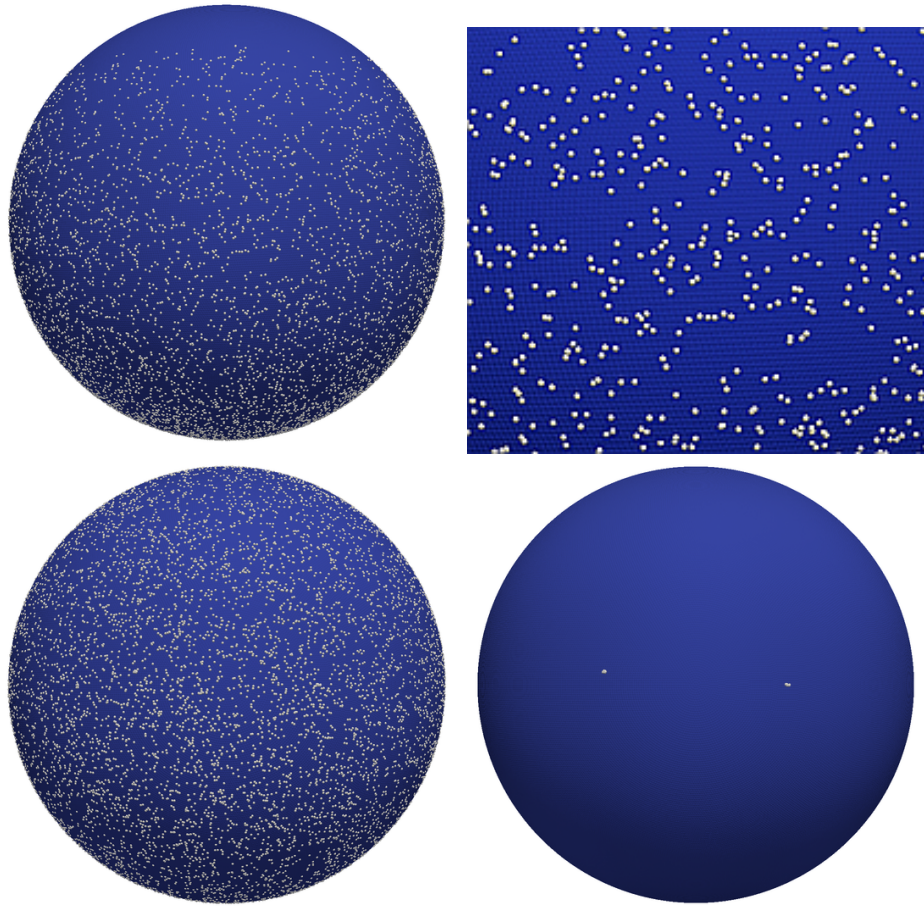


Figure 3: A spherical grid in equatorial coordinates (in blue) with 12000 randomly generated events and two point-like sources (in white). The grid-points are rendered with a radius of about 0.5° , hence they overlap and form a closed sphere. Only the hemisphere of the three dimensional sphere facing the observer is visible in this near-side general perspective projection. Top left: View on the equator (declination of 0°). Top right: Zoom to centre. Bottom left: View from below to the south pole (declination of -90°). Bottom right: The same setup displayed without the random events. All following spheres are oriented as the bottom spheres with the view from a declination of -90° .

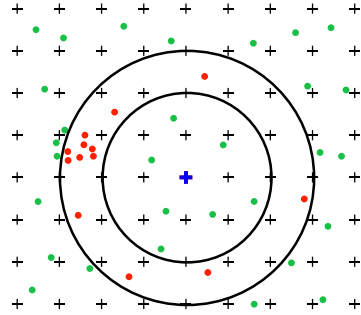


Figure 4: Scheme of the neutrino counting. Crosses mark the gridpoints with a distance of 0.5° between them. Green and red dots correspond to neutrinos. The blue cross is the gridpoint that is being evaluated. The current search scale (here 1.0° to 1.5°) is defined by the black circles. Neutrinos which are counted with the current search scale at the current searchpoint are shown in red. The result of the evaluation of this scale at the blue gridpoint is 13.

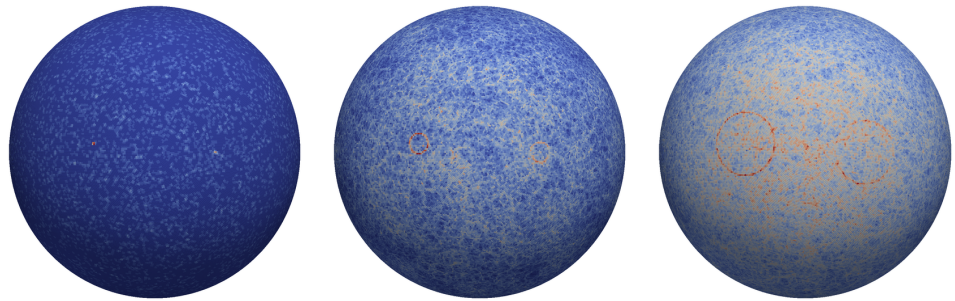


Figure 5: Left: The spherical search grid after counting events in a ring between 0.0° and 0.5° around each gridpoint. Middle: Result of the counting step between 3.0° and 3.5° . Right: Result of the counting step between 10.0° and 10.5° . The colour code is readjusted between the different scales.

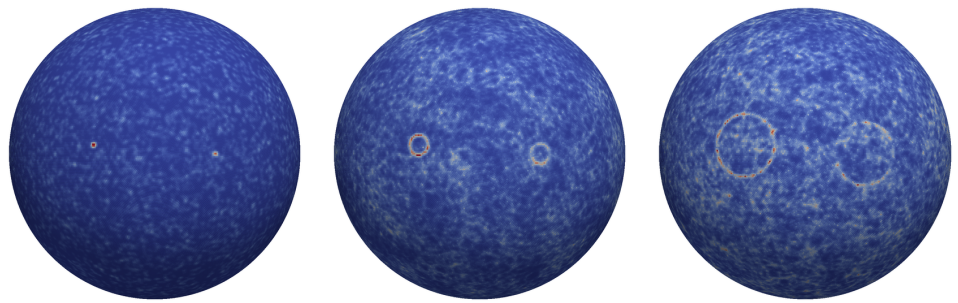


Figure 6: Left: Colour coded R values as defined in Section 4.3 on the grid for the scale 0.0° to 0.5° . Middle: 3.0° to 3.5° . Right: 10.0° to 10.5° .

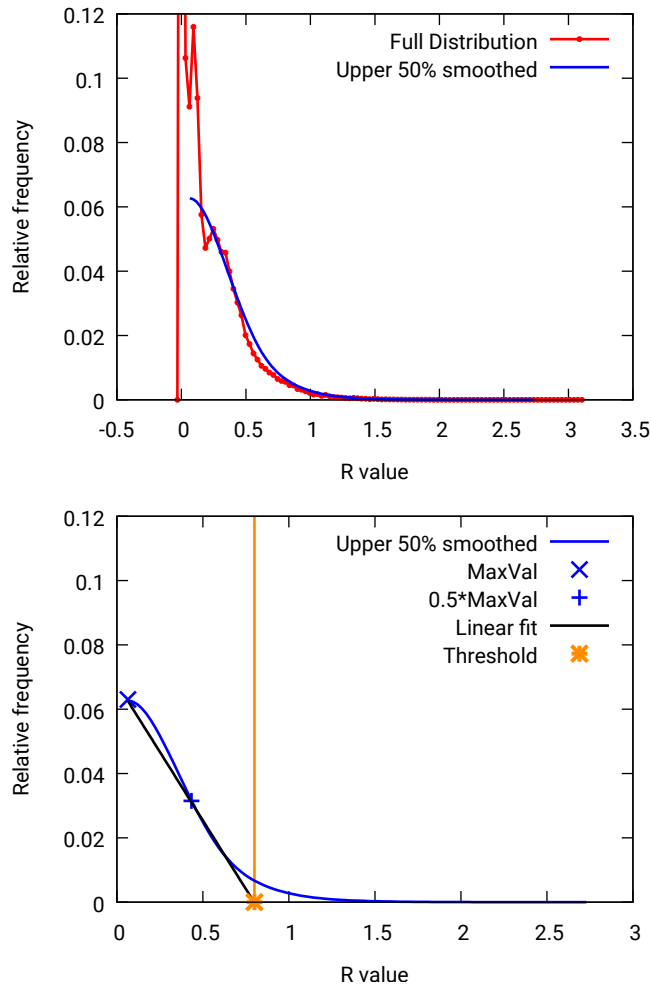


Figure 7: Top: The histogram of R values for one scale (0.0° to 0.5° in this example) is shown in red. Starting from the median value, the histogram is smoothed by Gaussian smearing to obtain the blue curve. Bottom: The threshold θ is determined by the zero-crossing of the line through the point with the maximum y-value on the blue curve and the point with half this y-value.

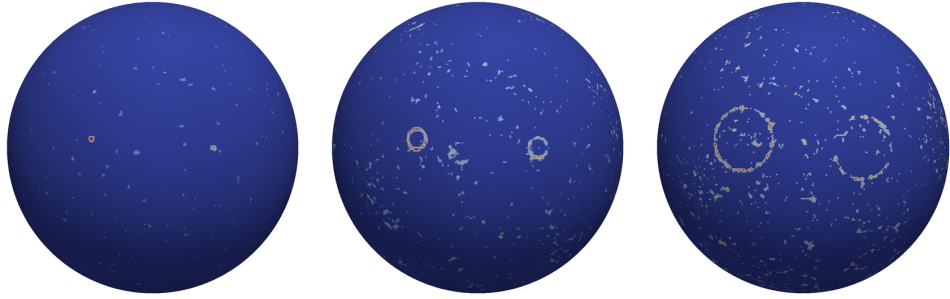


Figure 8: Left: Values of E after the segmentation step as given by Equation 2 on the spherical grid for the scale 0.0° to 0.5° . Middle: 3.0° to 3.5° . Right: 10.0° to 10.5° .

4.5 Remapping

The next step is to reconstruct the original location of the neutrinos that caused the remaining high values of E on the spheres. The values for a search scale d originated from counting neutrinos that are between d and $d + 0.5$ degrees away from the gridpoints where the values are stored. S_p is the set of gridpoints with a distance between d and $d + 0.5$ degrees around a gridpoint p . N_p is the number of gridpoints in S_p . The current value E_p of a gridpoint p is then distributed evenly to all these gridpoints. The result for each gridpoint is then given by:

$$A_p = \sum_{q \in S_p} \frac{E_q}{N_q} \quad (3)$$

This step maps the information back to all potential origins, meaning all gridpoints where the neutrinos contributing to the value could have been located. The results of these computations are shown in Figure 9. A higher density in the original neutrino distribution is now encoded in the overlapping pattern of the remapped circles, see middle and right of Figure 9.

4.6 Summation

Having evaluated multiple approaches to exploit the information available in the multitude of scales, a simple sum of the scales to one spherical grid was found to allow the most robust evaluation. Since the influence of random fluctuations is high for the smallest scale, it is not included in this sum. Equation 4 explicitly introduces the index i that denotes the distance scale for a variable⁴. This index has been omitted in the previous equations as

⁴For a scale i the search distance $d = (i - 1) \cdot 0.5^\circ$

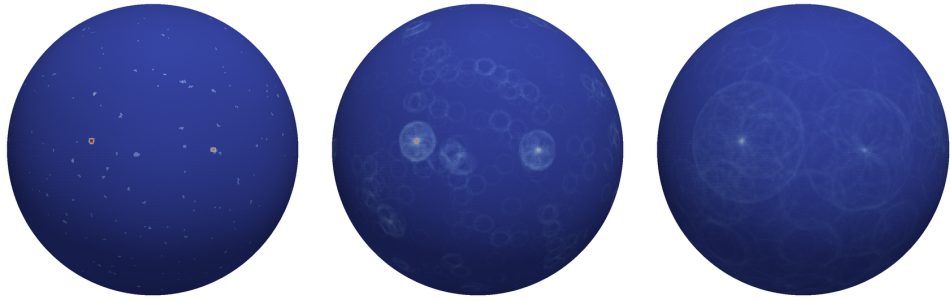


Figure 9: Left: Values of A after the remapping step as given by Equation 3 for the scale 0.0° to 0.5° . Middle: 3.0° to 3.5° . Right: 10.0° to 10.5° . Note that the colour code is the same for these three spheres.

the variables for all computations have been within the same distance scale.

$$S_p = \sum_{i=2}^{180} A_{p,i} \quad (4)$$

The result of the summation can be seen in Figure 10.

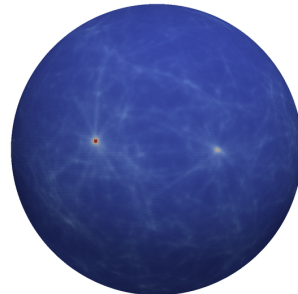


Figure 10: The sum of the search scales as given by Equation 4.

4.7 Segmentation II

Identifying connected regions of high values on the final single sphere, which could be linked to neutrino sources, is again achieved by a segmentation as already described for the individual scales in Section 4.4. The same procedure is used, but this time with the option to obtain different thresholds θ_β by scaling the distance between the minimum non-zero value found on the sphere S_{\min} , and θ , the threshold computed in the previous segmentations, using a factor $\beta \in \mathbb{R}$. A new threshold is then given by:

$$\theta_\beta = S_{\min} + \beta(\theta - S_{\min}) \quad (5)$$

The outcome of the segmentation using β for each gridpoint p is then given by:

$$F_p = \begin{cases} S_p, & S_p \geq \theta_\beta \\ 0, & S_p < \theta_\beta \end{cases} \quad (6)$$

Lower values for β result in lower thresholds θ_β , allowing more extended structures to be found, while higher values only preserve the high peaks, favouring smaller morphologies. The results are then filtered using a two-dimensional median filter to suppress potential artefacts (e.g. single gridpoints). The effect of different thresholds for the segmentation is visualised in Figure 11. Up to this point no explicit bias for any source property is included in this search. Based on an evaluation of a variety of simulated sources, two values have been set: $\beta = 0.75$ and $\beta = 1.11$. These values are chosen to be more sensitive to extended than small or point-like structures, since ANTARES has conducted dedicated, location independent searches for point-like sources already [26], but not for extended sources or a clustering of small structures without predefined location or size.



Figure 11: The effect of different thresholds on the segmentation. Left: F values as given by Equation 6 for $\beta = 0.75$, Middle: $\beta = 0.95$, Right: $\beta = 1.11$.

A connected group of gridpoints, all with values above θ_β , is called a cluster.

4.8 Significance

The final step is to distinguish potentially significant clusters from random accumulations. Since the exact size, shape, position and composition of a cluster is highly unlikely to be reproduced using pseudo experiments, more generic metrics must be used to evaluate the significance of a cluster. Many metrics have been designed and tested on a multitude of simulated sources [21], each with different sensitivities to different sources. No single metric can be maximally sensitive to all potential sources. But increasing the number of metrics in the analysis also means that a higher trial factor has to be taken into account. Motivated by the fact that ANTARES has already

conducted specialised searches for small and point-like sources, the metric “clustersize”, given by the number of gridpoints N in a cluster, has been chosen, performing best for more extended sources.

The significance for each cluster is then derived from pseudo experiments with scrambled events as explained in Section 4.3. For each threshold θ_β (and each metric when multiple metrics are used), the distribution obtained from the pseudo experiments has to be treated independently, as e.g. the distribution of the sizes of clusters depends on the used threshold. A pre-trial p-value and hence a pre-trial significance is computed for each observed cluster using the corresponding distribution. The distribution of the values obtained for the metric “clustersize” (in gridpoints) for a threshold using $\beta = 0.75$ is shown in Figure 12. A fit to the data is used instead of the tail of the distribution where the significance would be limited by the available statistics. For each pseudo experiment only the highest pre-trial significance

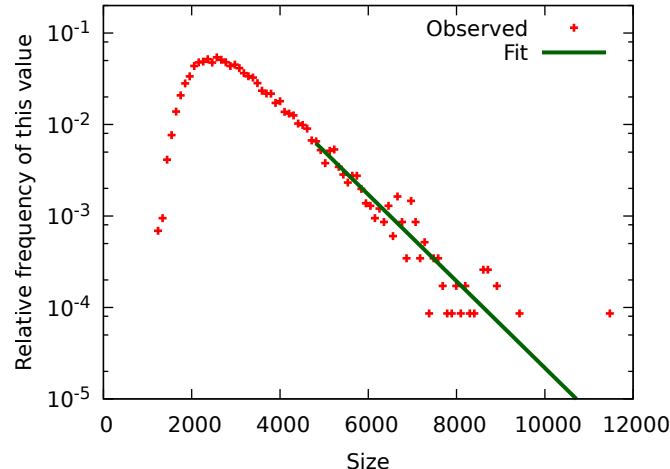


Figure 12: The distribution of the sizes of clusters from pseudo experiments and a fit to the tail of the distribution.

of any cluster from any threshold (and any metric) is considered the result of this pseudo experiment. The post-trial significance is then obtained by a comparison of the measured pre-trial significance of an observed cluster with the distribution obtained from pseudo experiments.

4.9 General considerations

To illustrate the behaviour of the method for another type of artificial source, Figure 13 shows a setup with an extended source instead of the two point sources. It can be seen that the location and size are approximated reasonably well, but, especially with lower thresholds, additional filaments extend

from the actual shape where random accumulations of background neutrinos occurred. More examples, also for asymmetric shapes, can be found in [21].

The sensitivity of this method for deviations from a homogeneous spatial distribution is different compared to previously used algorithms. For instance, the two-point correlation analysis [27] is more sensitive to a scenario where many faint sources with the same extension are distributed evenly throughout the sky. On the other hand, the multiscale search is considerably more sensitive in scenarios that include a spatial clustering of these faint sources. It also benefits more from the presence of one or more dominant sources. While the true nature of the sources of high-energy cosmic neutrinos is still unknown, this algorithm offers a high sensitivity for a very wide range of possible scenarios. This in particular includes the recently favoured scenario in which many faint sources dominate the observed diffuse flux [28].

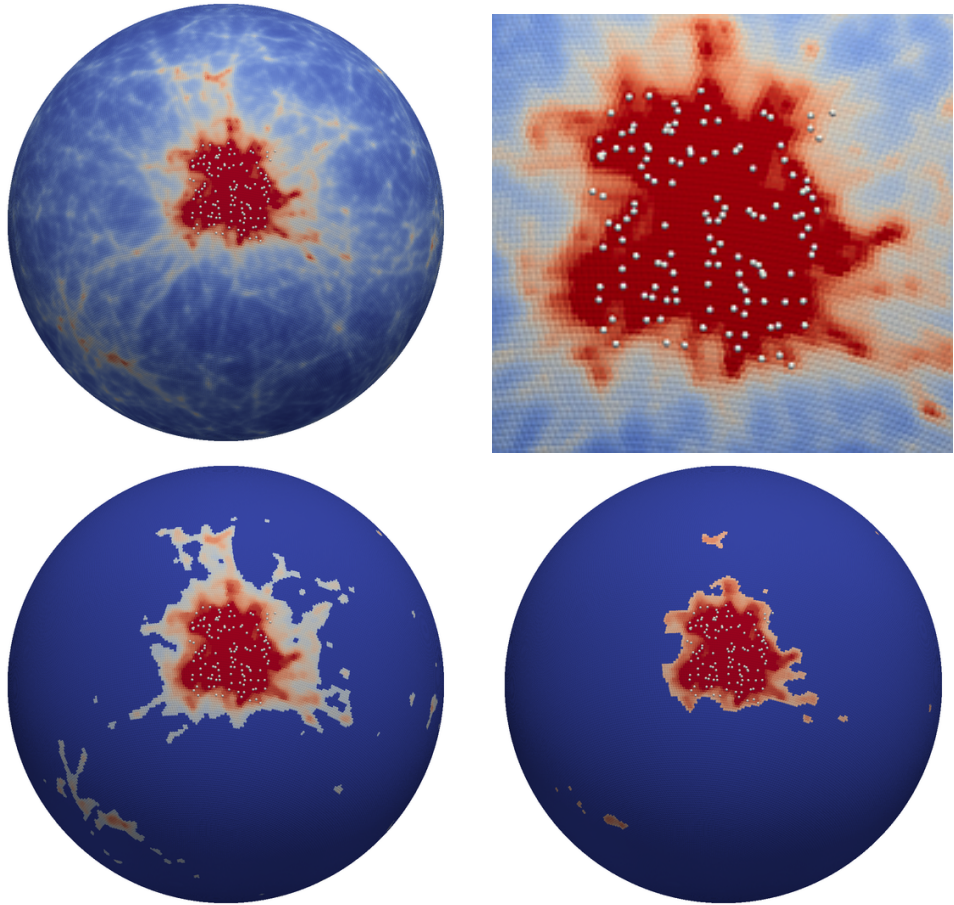


Figure 13: Top left: An illustrative example for the behaviour of the method for an extended source, 20° by 20° . The additional 120 source neutrinos are depicted in white. The 12000 background neutrinos are not rendered. Colour indicates the values after the summation, corresponding to Figure 10. Top right: A zoom to the source region. Bottom: The images depict the results after segmentations using $\beta = 0.75$ and $\beta = 1.11$, corresponding to Figure 11, left and right.

5 Results

This analysis was performed following a data blinding concept. That means that the development of all methods presented in Sections 2, 3 and 4 and the optimisation of all cuts had been completely finished before the recorded data sample was processed. The small data sample that had been used to verify the methods was excluded from the final sample.

5.1 ANTARES

Using the methods described in Sections 2 and 3, the evaluation of the ANTARES data from 2007 to 2012 results in 13283 candidates for charged current muon neutrino events, with an expected number of background neutrinos of 13078 ± 362 (statistical error) from interactions of cosmic rays in the atmosphere. Applying the multiscale search method described in Section 4 yields the result shown in Figure 14. Using the higher segmentation threshold $\beta = 1.11$, no cluster with a significance above 0.8σ has been found. With $\beta = 0.75$ a very large structure is found. After accounting for all known systematic effects, the large structure, called “the cluster” from here on, has a post-trial significance of 2.5σ . Its size is 13312 connected gridpoints, equivalent to about 3328 degree² or 8% of the sky. Even if not significant on its own, this structure constitutes an interesting feature in the data which is worth further studies. It can be noted that the cluster contains the Galactic Centre, which is located in the centre of the presented skymaps in galactic coordinates. More details on the inner structure of these clusters can be seen in Figure 15, which shows the result of the summation of all scales before the segmentations. It should be noted that with the limited available statistics, random fluctuations do influence the results.

5.2 IceCube IC40

In order to perform an independent cross check of the result obtained using ANTARES data, the publicly available IC40 dataset [29] published by the IceCube Collaboration has also been analysed. This analysis searches specifically for an excess in the area of the large cluster found in ANTARES data. To achieve this, it only considers clusters found in the IC40 data that overlap with the ANTARES cluster by at least 51% of their area. The value of 51% is chosen here because requiring an overlap of close to 100% would exclude e.g. clusters that extend beyond the shape of the ANTARES cluster.

Since the requirement for overlap implicitly confines the size of the cluster, the clustersize in gridpoints N is no reasonable metric to assess the significance of a cluster in this evaluation. Therefore the metric that gave the second best results in the investigations introduced in Section 4.8 has

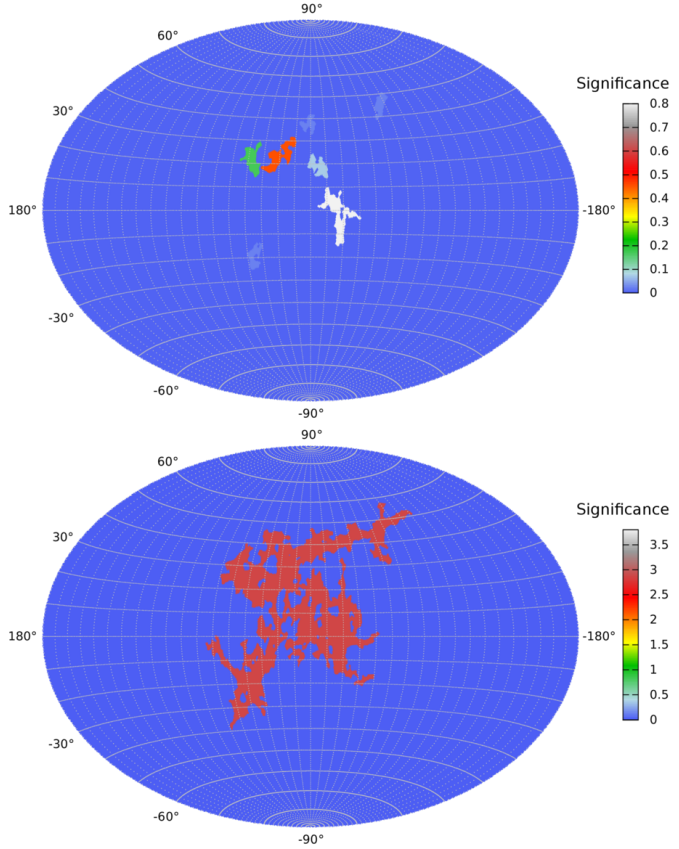


Figure 14: The result of the multiscale search for ANTARES data. The skymap is a Hammer-Aitoff projection of the resulting sphere in galactic coordinates. The colour code of the clusters indicates the post-trial significance in units of σ . Top: using $\beta = 1.11$ for segmentation. Bottom: Using $\beta = 0.75$.

been used. It is the mean value of the \sqrt{N} gridpoints⁵ with the highest values within a cluster.

The result obtained by this adapted search on the IC40 data set is shown in Figure 16. A cluster is found within the expected shape with a post-trial significance of 2.1σ .

The observation that not all features in the skymaps in Figures 15 and 16 match exactly is to be expected, as ANTARES has its highest sensitivity at lower energies compared to IceCube. Moreover, random fluctuations of atmospheric neutrinos do influence the results. The position of the found cluster overlaps with the search template by 78% of its size and partially with

⁵Rounded to the nearest integer number

the positions of the only two clusters that are located within the common field of view of ANTARES and IceCube, as seen comparing Figures 14 and 16 (red and green clusters for $\beta = 1.11$).

6 Conclusions

Two new data processing techniques that enhance the selection and reconstruction accuracy for the resulting sample of neutrino candidates, and a novel analysis method have been presented. The analysis method allows sources of arbitrary location and morphology to be detected without relying on a neutrino source model. It is worth noting that the underlying ideas of Selectfit, combining algorithms for similar tasks using classification, as well as of the model-independent multiscale source search, do not rely on the properties of ANTARES or even of neutrinos. Hence they can be used for many similar tasks, also in other experiments.

Applied to ANTARES data recorded between 2007 and 2012, this analysis found a large structure with a post-trial significance of 2.5σ . This result is consistent with a random fluctuation of the background of atmospheric neutrinos. Using this method to analyse public data from IceCube resulted in an excess located within the overlap between the cluster from the ANTARES data and the field of view of IceCube. This observation has a significance of 2.1σ .

Even though a general, model-independent analysis cannot be as sensitive as a dedicated search due to the high trial factors, this method provides a good way to become aware of the most prominent and even unforeseen structures in data and can be regarded as a trigger for more specific investigations.

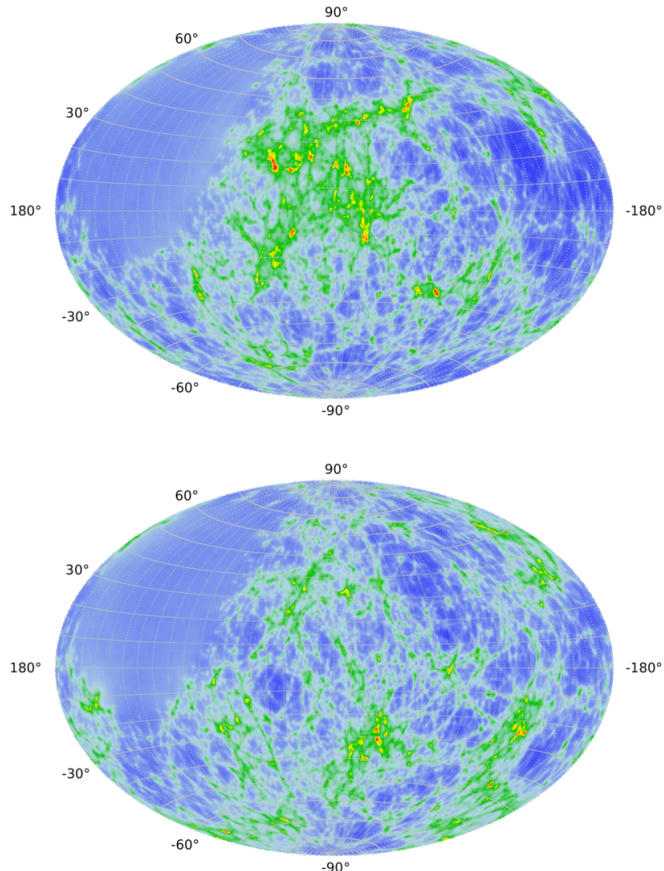


Figure 15: Top: Sum of all evaluated scales (corresponding to Figure 10, not directly to the neutrino flux) resulting from ANTARES data, in galactic coordinates and before segmentations. As only upgoing events are used in this analysis, the field of view of ANTARES does not cover the whole sky. This results in the large, homogeneously blue area in the upper left of the skymap. Bottom: For comparison, an example for a random dataset with the same colour code as the ANTARES results. The observed maximum values of S , see Equation 4, are similar, while the clustering of the overfluctuations is more pronounced in the recorded data.

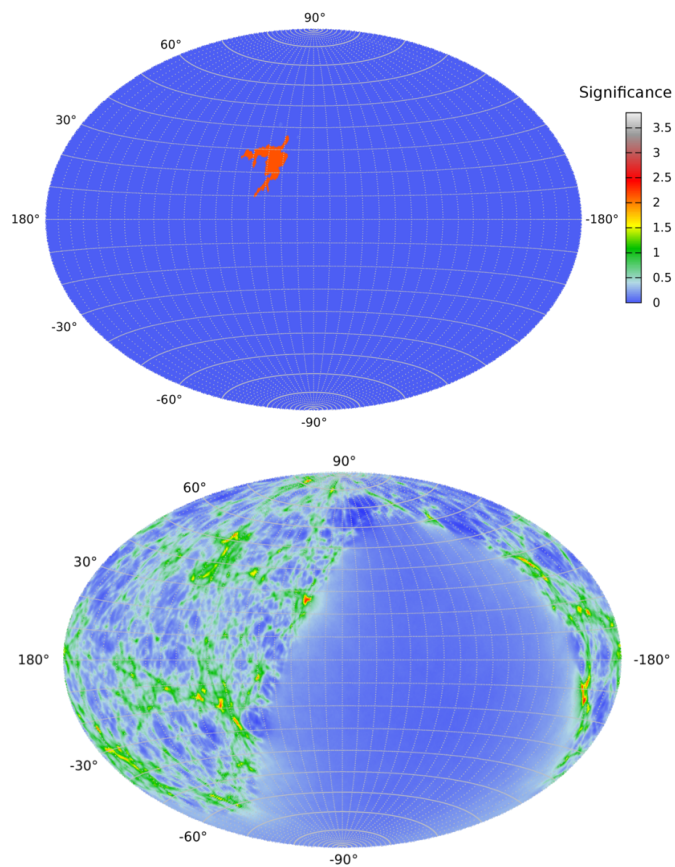


Figure 16: Top: The result on public IC40 data with segmentation using $\beta = 0.75$ in galactic coordinates. Bottom: The detailed structure of S -values behind the result on IC40 data before the segmentation.

7 Acknowledgments

The authors acknowledge the financial support of the funding agencies: Centre National de la Recherche Scientifique (CNRS), Commissariat à l'énergie atomique et aux énergies alternatives (CEA), Commission Européenne (FEDER fund and Marie Curie Program), Institut Universitaire de France (IUF), IdEx program and UnivEarthS Labex program at Sorbonne Paris Cité (ANR-10-LABX-0023 and ANR-11-IDEX-0005-02), Labex OCEVU (ANR-11-LABX-0060) and the A*MIDEX project (ANR-11-IDEX-0001-02), Région Île-de-France (DIM-ACAV), Région Alsace (contrat CPER), Région Provence-Alpes-Côte d'Azur, Département du Var and Ville de La Seyne-sur-Mer, France; Bundesministerium für Bildung und Forschung (BMBF), Germany; Istituto Nazionale di Fisica Nucleare (INFN), Italy; Stichting voor Fundamenteel Onderzoek der Materie (FOM), Nederlandse organisatie voor Wetenschappelijk Onderzoek (NWO), the Netherlands; Council of the President of the Russian Federation for young scientists and leading scientific schools supporting grants, Russia; National Authority for Scientific Research (ANCS), Romania; Ministerio de Economía y Competitividad (MINECO): Plan Estatal de Investigación (refs. FPA2015-65150-C3-1-P, -2-P and -3-P, (MINECO/FEDER)), Severo Ochoa Centre of Excellence and MultiDark Consolider (MINECO), and Prometeo and Grisolía programs (Generalitat Valenciana), Spain; Ministry of Higher Education, Scientific Research and Professional Training, Morocco. We also acknowledge the technical support of Ifremer, AIM and Foselev Marine for the sea operation and the CC-IN2P3 for the computing facilities.

References

- [1] M. G. Aartsen et al. First observation of PeV-energy neutrinos with IceCube. *Phys. Rev. Lett.*, 111:021103, 2013.
- [2] M. G. Aartsen et al. Evidence for High-Energy Extraterrestrial Neutrinos at the IceCube Detector. *Science*, 342:1242856, 2013.
- [3] M. G. Aartsen et al. Atmospheric and astrophysical neutrinos above 1 TeV interacting in IceCube. *Phys. Rev.*, D91(2):022001, 2015.
- [4] M. G. Aartsen et al. A combined maximum-likelihood analysis of the high-energy astrophysical neutrino flux measured with IceCube. *Astrophys. J.*, 809(1):98, 2015.
- [5] M. G. Aartsen et al. Evidence for Astrophysical Muon Neutrinos from the Northern Sky with IceCube. *Phys. Rev. Lett.*, 115(8):081102, 2015.

- [6] M. G. Aartsen et al. Observation of High-Energy Astrophysical Neutrinos in Three Years of IceCube Data. *Phys. Rev. Lett.*, 113:101101, 2014.
- [7] Andrii Neronov and Dmitry V. Semikoz. Evidence the Galactic contribution to the IceCube astrophysical neutrino flux. *Astropart. Phys.*, 75:60–63, 2016.
- [8] Andrii Neronov and Dmitry Semikoz. Neutrinos from Extra-Large Hadron Collider in the Milky Way. *Astropart. Phys.*, 72:32–37, 2016.
- [9] A. Neronov, D. V. Semikoz, and C. Tchernin. PeV neutrinos from interactions of cosmic rays with the interstellar medium in the Galaxy. *Phys. Rev.*, D89(10):103002, 2014.
- [10] S. Adrián-Martínez et al. Constraints on the neutrino emission from the Galactic Ridge with the ANTARES telescope. *Physics Letters B*, 760:143–148, 2016.
- [11] A. Neronov and D. V. Semikoz. Galactic and extragalactic contributions to the astrophysical muon neutrino signal. *Phys. Rev. D*, 93:123002, 2016.
- [12] S. Adrián-Martínez et al. Searches for Point-like and extended neutrino sources close to the Galactic Centre using the ANTARES neutrino Telescope. *Astrophys. J.*, 786:L5, 2014.
- [13] M. G. Aartsen et al. Searches for Extended and Point-like Neutrino Sources with Four Years of IceCube Data. *Astrophys. J.*, 796(2):109, 2014.
- [14] S. Adrián-Martínez et al. First combined search for neutrino point-sources in the Southern Hemisphere with the ANTARES and IceCube neutrino telescopes. *Astrophys. J.*, 823:65, 2016.
- [15] S. Adrián-Martínez et al. Searches for clustering in the time integrated skymap of the ANTARES neutrino telescope. *JCAP*, 1405:001, 2014.
- [16] M. G. Aartsen et al. Searches for small-scale anisotropies from neutrino point sources with three years of IceCube data. *Astropart. Phys.*, 66:39–52, 2015.
- [17] M. Ageron et al. ANTARES: The first undersea neutrino telescope. *Nucl. Inst. and Meth. A*, 656(1):11–38, 2011.
- [18] S. Adrián-Martínez et al. ANTARES Constrains a Blazar Origin of Two IceCube PeV Neutrino Events. *A&A*, 576:L8, 2015.

- [19] Bystritsky, V. and Bochkanov, S. (The ALGLIB Project). ALGLIB. <http://www.alglib.net>, 2011. 2011-11.
- [20] Tin Kam Ho. The Random Subspace Method for Constructing Decision Forests. *IEEE Transactions on Pattern Analysis and Machine Intelligence*, 20:832–844, 1998.
- [21] Stefan Geißelsöder. Model-independent search for neutrino sources with the ANTARES neutrino telescope. *Ph.D. thesis*, Friedrich-Alexander-Universität Erlangen-Nürnberg, 2016. http://www.ecap.nat.uni-erlangen.de/publications/pub/2016_Geisselsoeder_Dissertation.pdf.
- [22] L.A. Fusco et al. The Run-by-Run Monte Carlo simulation for the ANTARES experiment. *EPJ Web of Conf.*, 116:02002, 2016.
- [23] S. Adrián-Martínez et al. First Search for Point Sources of High Energy Cosmic Neutrinos with the ANTARES Neutrino Telescope. *Astrophys. J. Lett.*, L14:743, 2011.
- [24] J.A. Aguilar et al. A fast algorithm for muon track reconstruction and its application to the ANTARES neutrino Telescope. *Astropart. Phys.*, 34:652–662, 2011.
- [25] Erwin Lourens Visser. Neutrinos from the Milky Way. *Ph.D. thesis*, Universiteit Leiden, 2015. http://www.nikhef.nl/pub/services/biblio/theses_pdf/thesis_EL_Visser.pdf.
- [26] S. Adrián-Martínez et al. Search for Cosmic Neutrino Point Sources with Four Year Data of the ANTARES Telescope. *Astrophys. J.*, 760:53, 2012.
- [27] S. Adrián-Martínez et al. Searches for clustering in the time integrated skymap of the ANTARES neutrino telescope. *JCAP*, 05:001, 2014.
- [28] M. G. Aartsen et al. Neutrinos and Cosmic Rays Observed by IceCube. 2017. <http://arxiv.org/abs/1701.03731>.
- [29] R. Abbasi et al. A Search for a Diffuse Flux of Astrophysical Muon Neutrinos with the IceCube 40-String Detector. *Phys. Rev. D*, 84:082001, 2011. <http://icecube.wisc.edu/science/data/ic40>.